NANO LETTERS

pubs.acs.org/NanoLett Letter

Broadband Light Harvesting from Scalable Two-Dimensional Semiconductor Multi-Heterostructures

Da Lin, Jason Lynch, Sudong Wang, Zekun Hu, Rajeev Kumar Rai, Huairuo Zhang, Chen Chen, Shalini Kumari, Eric A. Stach, Albert V. Davydov, Joan M. Redwing, and Deep Jariwala*

Cite This: *Nano Lett.* 2024, 24, 13935−13944 Read Online

ACCESS | Metrics & More | Article Recommendations | Supporting Information

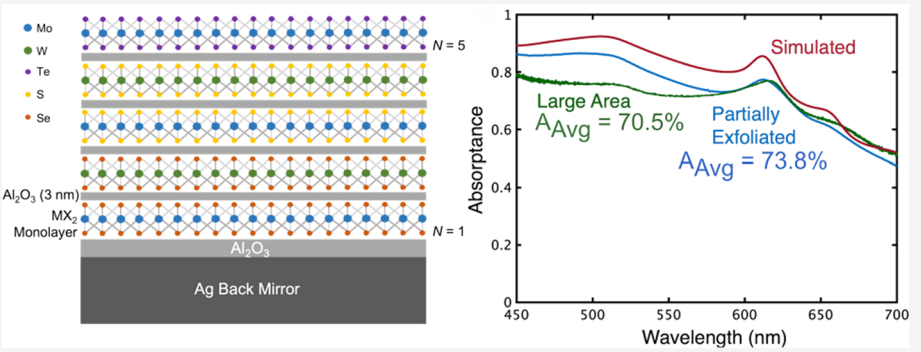

ABSTRACT: Broadband absorption in the visible spectrum is essential in optoelectronic applications that involve power conversion such as photovoltaics and photocatalysis. Most ultrathin broadband absorbers use parasitic plasmonic structures that maximize absorption using surface plasmons and/or Fabry−Perot cavities, which limits the weight efficiency of the device. Here, we show the theoretical and experimental realization of an unpatterned/planar semiconductor thin-film absorber based on monolayer transition-metal dichalcogenides. We experimentally demonstrate an average total absorption in the visible range (450−700 nm) of >70% using <4 nm of semiconductor absorbing materials scalable over large areas with vapor phase growth techniques. Our analysis suggests that a power conversion efficiency of 15.54% and a specific power >300 W g^{-1} may be achieved in a photovoltaic cell based on this metamaterial absorber.

KEYWORDS: *multiheterostructure, broadband absorber, photovoltaic, transition-metal dichalcogenide, nanophotonic*

Absorption occurs when light−matter interactions lead to an energy transfer from an incident photon to the irradiated material. In the context of optoelectronic devices, absorption is typically required to be either narrow-band (single wavelength) or broad-band (spectral) depending on the application. In the past decade, the field of thin-film, near-unity broadband absorption has garnered interest given its numerous benefits compared to bulk absorbers, such as decreased material usage and cost, shorter carrier collection distance that decreases recombination losses,[1] and decreased weight. While these characteristics open doors for the use of broadband absorbers for efficient ultrathin optoelectronic applications, such as photovoltaics,[2] photoelectrochemical processes,[3,4] and photodetection,[5] it is equally critical to continue innovating in the field of ultrathin broadband absorbing metamaterials, in and of itself, to pave the way for future device breakthroughs.

In the submicron range, the dominant approach to achieving broadband absorption has been engineering metamaterials using plasmonic nanocavities to generate localized surface plasmon−polaritons to strongly confine light in the absorbing material.[6] Metal−insulator−metal (MIM) structures were extensively studied with various plasmonic structures as the top layer.[7−10] Unfortunately, the energy absorbed by metals is lost through the thermalization of carriers, which is not useful and is often detrimental for optoelectronic devices. To combat this issue, thin-film semiconductors have been coupled to plasmonic nanostructures to enhance light−matter interaction.[11−13] However, employing metal plasmonic structures as the dominant mechanisms for strong light−matter coupling results in Joule heating losses in the metal; this parasitic absorption does not contribute to the optoelectronic function, decreasing the weight efficiency of the device. One strategy to avoid parasitic absorption in the metal nanostructures has been

Received: June 23, 2024
Revised: October 8, 2024
Accepted: October 9, 2024
Published: October 28, 2024

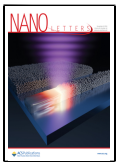

https://doi.org/10.1021/acs.nanolett.4c02963
Nano Lett. 2024, 24, 13935−13944

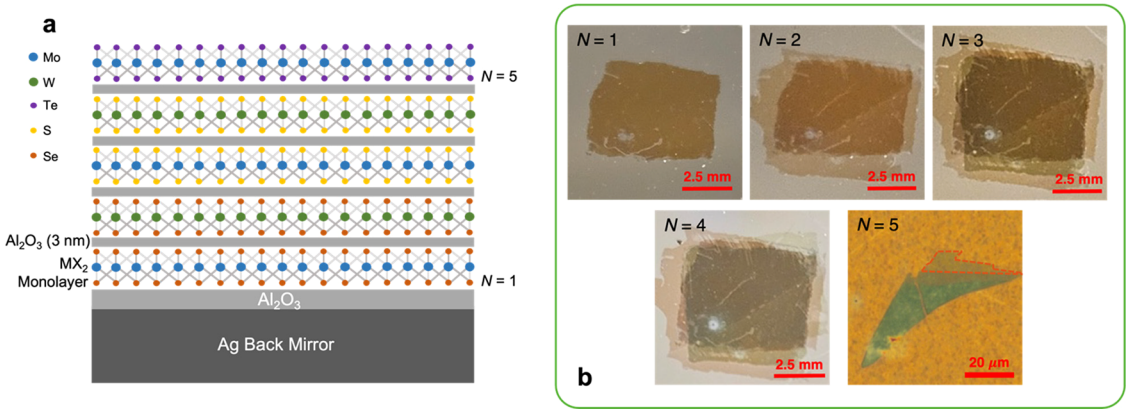

Figure 1. (a) Front-view schematic of an $N = 5$ TMDC multi-heterostructure composed of TMDC monolayers, dielectric spacers (Al_2O_3) with a bottom dielectric thickness of 33 nm, and a silver back reflector mirror. (b) Optical microscope (OM) images of the step-by-step fabrication process of an $N = 5$ large area sample.

to pattern the semiconductor itself to form cavity modes that couple to the incident light. Although this has been done to a 1 μm Si slab to achieve >80% absorption in the visible range,[14] it comes at the expense of scalability because of the complex patterning needed. Another strategy to increase the strength of light−matter interactions in a planar geometry is to alter the thickness of a layer to create a thin-film interference effect.[15,16] Absorption in planar semiconducting thin films on top of metal or metal/dielectric substrates has been demonstrated for $MoSe_2$,[17] Ge,[13,18] MoS_2,[19,20] and graphene.[21] While these studies concentrate most incident light into the semiconducting active layers, they do not push the boundary of ultrathin materials−the atomically thin limit−that would achieve the greatest energy efficiency by weight.

Previous work from our team has demonstrated near-unity narrowband absorption using a scalable multilayer superlattice structures based on atomically thin 2D transition-metal dichalcogenides (TMDCs) measuring <1 nm in thickness per layer,[22] and other recent work has demonstrated that a semi-transparent superlattice using four monolayers of active material can approach the absorption limit.[23] In this letter, we numerically and experimentally demonstrate a broadband visible absorber based on <4 nm of large area, scalable, planar (unpatterned) monolayer TMDCs. We achieve electronic isolation of each semiconducting layer within the multi-heterostructure stack to obtain multiple resonance peaks, contributing to a broadband absorption spectrum with an average total (sum of the absorptance of each layer) absorption in the visible range (450−700 nm) greater than 70%. This is the thinnest, scalable visible broadband absorber reported to date without the use of any bottom-up self-assembly, top-down nanopatterning, or integration of complex plasmonic nanostructures. We also simulate the potential photovoltaic performance of the multiheterostructure and find that it has a large potential specific power (>300 W g^{-1}). Our structure pushes the light−matter coupling efficiency limit of ultrathin semiconducting materials and is applicable for a plethora of optoelectronic devices.

Figure 1a illustrates our ultrathin visible broadband absorber design employing alternate layers of semiconducting (TMDC) monolayers and dielectrics (Al_2O_3), along with a back reflector (Ag). This geometry constitutes a multi-quantum well (MQW),[24] or multi-heterostructure, and it has been reported in our work that employed a single TMDC to enhance the narrowband absorption of a superlattice.[22] Monolayer TMDCs are chosen for the semiconductor layers because of their strong, quantum-confined excitons that are highly absorptive, their bandgaps that range from 1.1 to 2.0 eV, and their direct bandgap nature in the atomically thin limit which is highly desirable in optoelectronic applications.[25−31] Although the four bottom layers follow the trend of decreasing bandgap from top to bottom, which is typical in multitandem solar cells,[32] the smallest bandgap (2H-$MoTe_2$) is placed on the top. This is done to reduce the amount of degradation of $MoTe_2$ during fabrication since it is the most sensitive TMDC used to the ambient environment.[33,34] Simulations show negligible differences in absorption when the $MoTe_2$ is on the top or bottom of the SL since the overall thickness of the structure is much smaller than the wavelength of photons in the visible part of the spectrum (Figure S1a). Further simulations (Figure S1b) additionally indicate that other layer configurations, such as ordering in increasing bandgap from top to bottom, negligibly affect the total absorption of the system but do affect the absorption of individual layers due to optical screening. The Al_2O_3 insulating layers are 3 nm thick since previous studies of TMDC/insulator/TMDC heterostructures, using both a single[35] and two different types[36−38] of TMDCs, have shown the formation of interlayer excitons when the insulator is <3 nm thick. Interlayer excitons form as a result of the exciton wave function extending outward into multiple monolayers. Using a 3 nm thick insulator confines the wave function to a single monolayer, allowing for the preservation of monolayer properties.[39] The bottom dielectric underneath the SL strongly affects the light−matter interactions over a narrowband range because of its effect on interference within the SL. Because of this, the bottom dielectric function thickness is the only degree of freedom (DoF) that is used to optimize the broadband absorption of the system. The optimization process is done using the transfer matrix method (TMM) along with refractive index values measured using spectroscopic ellipsometry (Figure S2) to calculate the absorption of the multi-heterostructure. The refractive index of monolayer 2H-$MoTe_2$ was approximated as its bulk value (10 nm) because of a lack of the monolayer value in the literature.[40] The back mirror is 200 nm of E-beam evaporated Ag, which is far thicker than the penetration of visible light (14 nm @ λ = 500 nm). This ensures that no transmission occurs through the device, and absorption can be calculated directly from reflection ($A = 1 -$

https://doi.org/10.1021/acs.nanolett.4c02963
Nano Lett. 2024, 24, 13935−13944

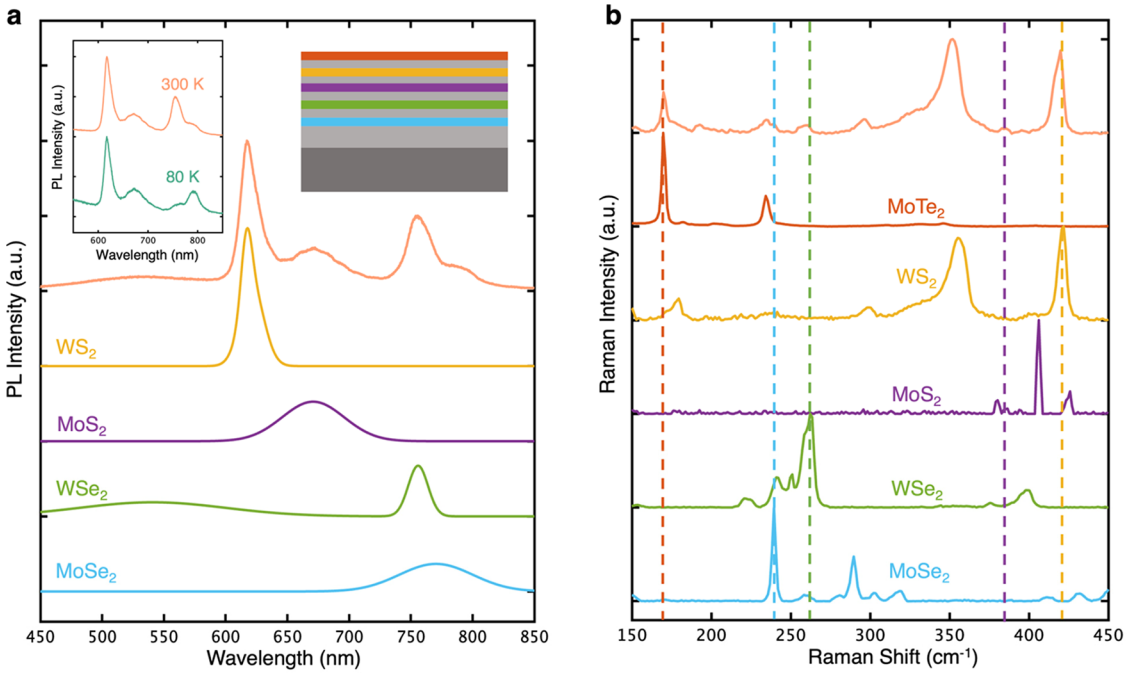

Figure 2. (a) Normalized photoluminescence (PL) spectra for the multi-heterostructure (orange) and deconvoluted Gaussian fits for individual layer PL spectra for the partially exfoliated multi-heterostructure. (b) Normalized Raman spectra for the multi-heterostructure matched with experimental Raman spectra for the CVD-grown/dry-transferred TMDC monolayer. Inset of (a): (left) temperature-dependent PL spectra for the multi-heterostructure at 300 and 80 K and (right) simplified front-view schematic of the multi-heterostructure.

R). Silver is chosen specifically to minimize parasitic absorption.[41]

One key advantage of using TMDC monolayers is the advent of techniques to isolate and deposit pristine monolayer TMDCs on any arbitrary surface on the wafer-scale,[42−44] as shown in Figure 1b. MOCVD is used to grow large area monolayer $MoSe_2$ (N = 1), WSe_2 (N = 2), WS_2 (N = 3), and MoS_2 (N = 4) on sapphire for the large area multi-heterostructure. However, for the partially exfoliated multi-heterostructure, $MoSe_2$ and WSe_2 are exfoliated. The films are then transferred to an optimized substrate using the wet transfer process to fabricate the multi-heterostructure (see the Supporting Information). The refractive index is found to be unaffected by the wet transfer process, so the total absorption of the multi-heterostructures is unaffected by the potential damage of the transfer process (Figure S3).

Monolayer $MoTe_2$ (N = 5) is mechanically exfoliated from a bulk crystal using a PDMS stamp technique.[44] As demonstrated in subsequent sections, both techniques of transfer yield high-quality samples with minimal defects, with the N = 4 SL demonstrating exemplary environmental stability. Atomic layer deposition (ALD) is used to deposit thin-film Al_2O_3 on top of the back reflector and between the monolayer TMDC layers. Figure S4 demonstrates a separate realization of the multi-heterostructure stack using mechanically exfoliated $MoSe_2$ (N = 1), WSe_2 (N = 2), and $MoTe_2$ (N = 5) and MOCVD grown WS_2 (N = 3) and MoS_2 (N = 4). It is important to note that all of the TMDC monolayers have been grown on the wafer-scale using MOCVD, demonstrating the scalability of our system.[45−47] In Figure S5, TEM images and EDS maps are captured, where the individual layers and identities of the multi-heterostructure stack can clearly be seen. Further details on the experimental process may be found in the Supporting Information.

A distinctive feature of monolayer TMDCs from their multilayer counterparts is their strong photoluminescence (PL), which is a result of the indirect to direct bandgap transition in the monolayer limit.[48,49] Interlayer coupling causes multilayer TMDCs to suffer from increased non-radiative recombination that quenches the intensity of the PL, reducing their potential optoelectronic efficiency.[36,50] In Figure 2a, we verify the monolayer thicknesses and electronic isolation of the fabricated TMDC layers within our SL through PL measurements of a characteristic N = 5, partially exfoliated SL (WSe_2, $MoSe_2$, and $MoTe_2$ were mechanically exfoliated while the MoS_2 and WS_2 are large area and were transferred using a wet transfer process). The resulting peaks are generally red-shifted from the A exciton resonance energy for the identified monolayer TMDC due to phonon energy loss in radiative recombination, and all of the peaks are within 50 meV of prior measurements.[27−30,51] Variations are attributed to mechanical strain introduced to the SL during the extensive fabrication process,[28,52] as well as additional dielectric screening from the surrounding environment that decreases the electronic bandgap of the TMDC.[53] This is particularly relevant for the bottom layer, $MoSe_2$, which has the largest deviation from previous works while also experiencing the most mechanical mismatch, environmental contamination, and dielectric encapsulation. The blue-shift of the peak, in particular, can be attributed to a strong in-plane compressive stress[52] placed on the monolayer as a result of eight additional layers on top of it. This blue-shift is observed throughout the fabrication process (Figure S6). The relative intensities of the peaks (WS_2, WSe_2, MoS_2, $MoSe_2$) are consistent with the simulated absorption of the monolayers at 405 nm (Figure S7) and experimentally demonstrated PLQY values.[44,54−56] The main exception to this trend is $MoSe_2$, which performs significantly worse than expected in comparison to the other TMDCs; this

https://doi.org/10.1021/acs.nanolett.4c02963
Nano Lett. 2024, 24, 13935−13944

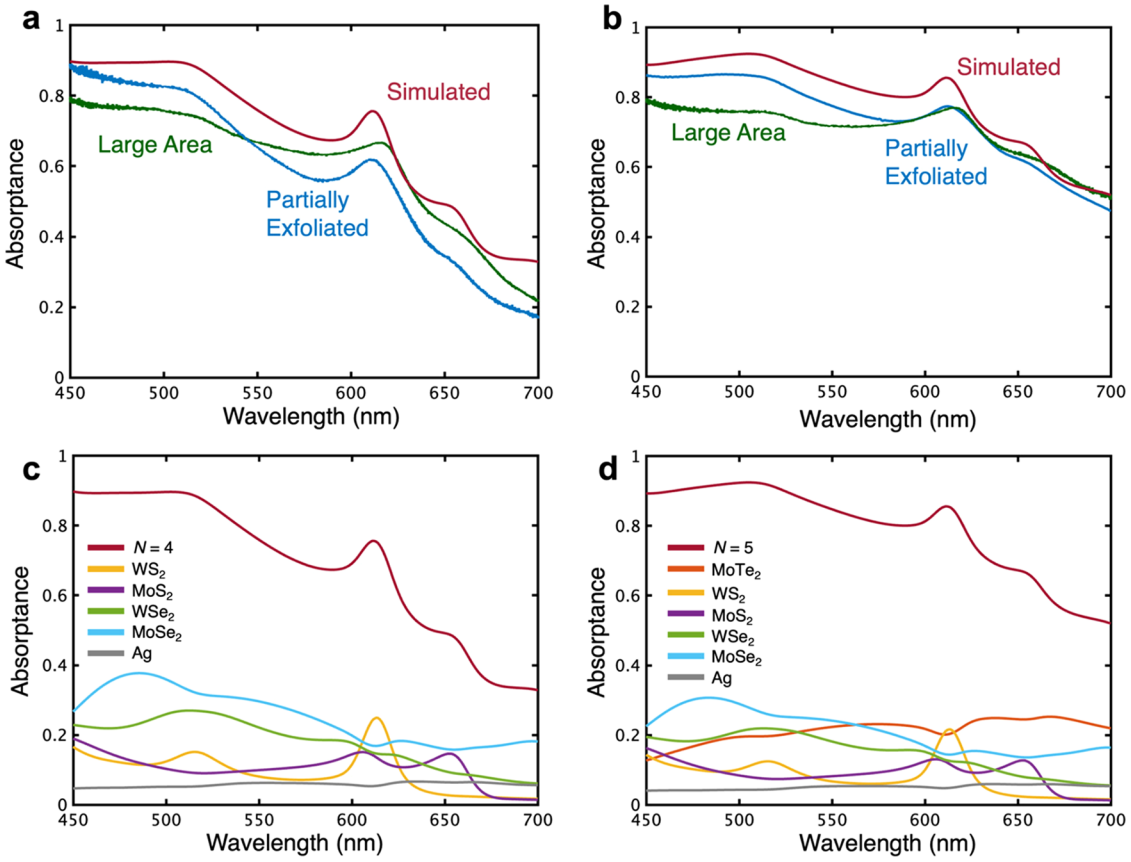

Figure 3. Measured and calculated total absorption spectra from 450 to 700 nm at normal incidence for the (a) $N = 4$ and (b) $N = 5$ multi-heterostructure, and the corresponding (c and d) calculated layer-by-layer total absorption spectra.

is attributed to increased defect states and strains introduced in the fabrication process, as outlined above, as well as the screening of photons as they travel through multiple interfaces in the SL to the collector. The MoX_2 (X = S, Se) peaks are also observed to have larger full width at half maximums (fwhm's) compared to their WX_2 (X = S, Se) equivalents by 27 and 51 nm, respectively. This behavior is expected for MoS_2, which inherently scatters more energy to phonons than WS_2,[57] as well as for $MoSe_2$, where increased localized defect scattering combines with the A exciton peak.[58]

We further probe the photoluminescence behavior of our multi-heterostructure by taking low temperature (LT) measurements of the SL at 80 K, as shown in the inset of Figure 2a and deconvoluted in Figure S8. The most notable shifts in PL resonance are in the MoS_2 peak, which experiences a red-shift of 25 meV, and $MoSe_2$, with a red-shift of 45 meV. The red-shifting is a result of the thermal expansion coefficient mismatch between layers, changing the stress in the TMDC layers and counteracting the typical effects of cooling.

The WS_2 and WSe_2 experience negligible shifts. These peaks shift as temperature decreases, and this can be attributed to increased thermally induced tensile stress.[28] $MoSe_2$ experiences the largest thermally induced tensile stress because it has the highest coefficient of linear thermal expansion among the TMDCs and dielectric materials, while MoS_2 is the second highest.[59−63] Conveniently, the defects in $MoSe_2$ caused by the initial compressive stress at 300 K is relieved as the temperature is decreased, increasing the relative intensity of the $MoSe_2$ PL compared to WSe_2.

The identity and thickness of the monolayers are further confirmed using Raman spectroscopy (Figure 2b), which plots the Raman spectra for an $N = 5$ SL against experimentally acquired Raman spectra for CVD-grown or mechanically exfoliated monolayers. Thickness-dependent Raman spectra is highly accurate in pinpointing layer-by-layer increases in thickness due to additional interlayer vdW interactions that stiffen the A_{1g} mode from the increased vibration restoring force, as well as stacking effects that relax the E_{2g} mode from shifting lattice dimensions.[64,65] As seen, the top two layers are easily discernible in the $N = 5$ spectra; the A_{1g} modes for monolayer $MoTe_2$ and WS_2 closely match those of previously acquired values.[31,65] The bottom layers are more difficult to identify due to background noise attributed to interfacial screening; however, layer-by-layer measurements of an $N = 3$ SL clearly identified A_{1g} and E_{2g} peaks corresponding to monolayer values (Figure S9).[30,66]

Figure S10 demonstrates equivalent data in the representative $N = 5$, large area SL depicted in Figure 1b, where electronic isolation is clearly demonstrated in the photoluminescence and Raman measurements.

The absorption spectra are obtained experimentally for a characteristic $N = 4$ and $N = 5$ SL for both large area and partially exfoliated samples (Figures 3a and 3b). Absorption is calculated as 1 − reflection, given that the Ag back reflector blocks all transmission. The multilayer reflections within the SL lead to a broadband, multiresonant peak absorption spectrum within the visible range (450−700 nm). An average total absorption of 58.5% and 73.8% is achieved for the partially exfoliated $N = 4$ (active thickness = 2.8 nm) and $N =$

https://doi.org/10.1021/acs.nanolett.4c02963
Nano Lett. 2024, 24, 13935−13944

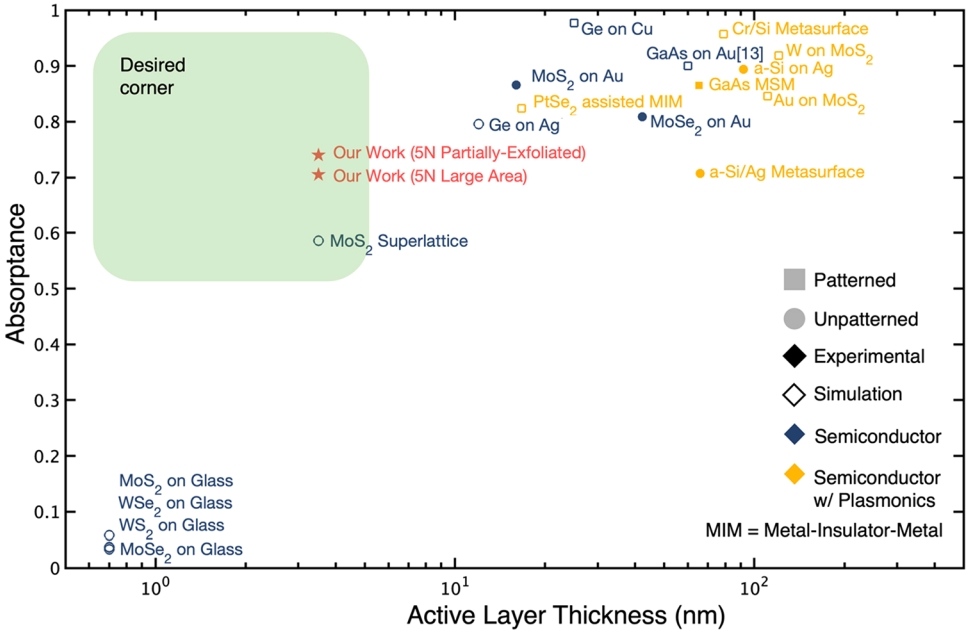

Figure 4. Benchmark of our absorber against other absorbers according to estimated absorptance and active layer thickness based on metrics of dominant absorbing material, patterning, and study type.[11,12,17,19,74−82]

5 SL (active thickness = 3.5 nm), respectively, while an average total absorption of 60.6% and 70.5% is achieved for the large area N = 4 and N = 5 SL. Further, in the 450−520 nm range, the partially exfoliated N = 5 SL demonstrates >80% average total absorption while the large area N = 5 SL demonstrates >75% average total absorption. The visible broadband absorption is attributed to a combination of the strong excitonic resonance peaks of the individual semiconducting layers and an enhancement of light−matter interactions from the optimized thickness of the bottom dielectric. The first resonant peak at 516 nm is attributed to the B exciton peak of WS_2.[67] A and B exciton peak splitting is well-documented and is attributed to the splitting of the valence band due to spin−orbit coupling.[68] The second resonance peak at 614 nm is predominately the A exciton peak of WS_2 and the B exciton peak of MoS_2, while the third resonance peak at 653 nm corresponds to the A exciton of MoS_2. Figure S11 additionally shows experimental resonance peaks at 745 nm from the WSe_2 A exciton and 788 and 704 nm from the $MoSe_2$ A and B excitons, respectively, in the partially exfoliated sample. Solar absorption under 1.5 AM solar irradiation is calculated as shown in Figure S12.

The absorption of our SL is simulated using the TMM[69] to verify that our experimental results are consistent with theoretical models. The simulated absorption spectra in Figures 3a and 3b were found to agree well with the partially exfoliated sample, while variations in the large area sample are attributed to introduced impurities and defects in the growth and wet transfer process. We verify that the broadband visible absorption of the SL has been optimized using a constrained minimization algorithm where the bottom dielectric thickness t is varied, resulting in t = 33 nm for the N = 4 multi-heterostructure and t = 31 nm for the N = 5 multi-heterostructure. For the sake of experimental fabrication, 33 nm alumina was deposited for the sample device presented in this text.

The TMM model for our SL allows for the layer-by-layer analysis of our structure (Figures 3c and 3d). The average total broadband visible absorption, in descending order, of the N = 4 (68.77%) model is $MoSe_2$ (25.28%), WSe_2 (17.79%), MoS_2 (10.56%), WS_2 (9.38%), and Ag (5.76%) while that for the N = 5 (79.19%) model is $MoTe_2$ (21.37%), $MoSe_2$ (21.03%), WSe_2 (14.85%), MoS_2 (8.93%), WS_2 (7.94%), and Ag (5.06%). Layer absorption is particularly enhanced in the bottom layer of the SL, where absorption values surpass the values expected from freestanding, electronically isolated monolayers.[70,71] A close fit exists between the experimental result and the layer-by-layer predicted excitonic resonances, which further confirms the consistency of the SL.

We benchmark our N = 5 SL against other ultrathin broadband absorbers in the field in Figure 4 by comparing average absorption in the 450−700 nm range and effective active layer thickness. Further details about how the effective thickness and absorption are calculated are found in the Supporting Information. We compare our SL to geometries ranging from plasmonic metasurfaces to planar semiconductors. Our multi-heterostructure is found to have the record average absorption in the visible range per nanometer of active layer thickness (21.1% nm^{-1} for the partially exfoliated sample and 20.1% nm^{-1} for the large area sample). As seen, while various metal-based absorbers have achieved near-unity broadband absorption within the visible range, they require metals that are thicker than the penetration depth of the metals (10 to 100 nm typically). Additionally, the photocarriers in the metals lose all of their energy to thermalization. Therefore, plasmonic metasurfaces are best suited to thermal applications. While plasmonic nanostructures can be used to effectively control and guide light to the underlying semiconductor layer, parasitic absorptions in the metal reduce the efficiency of the interaction while increasing the total effective thickness/weight of the absorber. In addition, the need to pattern plasmonic nanostructures is a key obstacle in realizing many semiconductor-metal-coupled absorbers for widespread optoelectronic use; lithographic steps are costly, timely, and technically difficult to realize and scale. Our multi-heterostructure can overcome these two key obstacles in achieving ultrathin

https://doi.org/10.1021/acs.nanolett.4c02963
Nano Lett. 2024, 24, 13935−13944

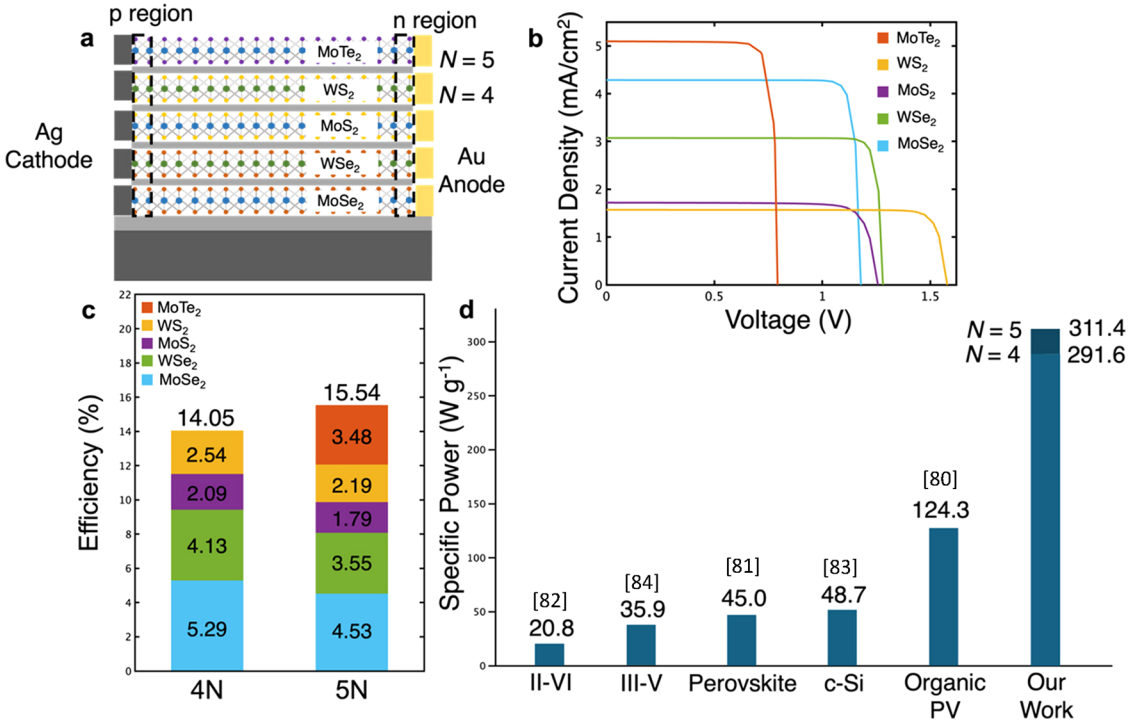

Figure 5. (a) Schematic of the separate-contact model for a photovoltaic (PV) cell based on the multi-heterostructure absorber. (b) Calculated I–V curves for the $N = 5$ separate contact model. (c) Layer-by-layer calculated photon conversion efficiency (PCE) based on the $N = 4$ and $N = 5$ multi-heterostructure PV. (d) Benchmark of the specific power of the $N = 5$ multi-heterostructure PV against leading ultrathin PV materials with estimated effective thicknesses.[84−88]

optoelectronic devices by confining absorption almost entirely in the semiconducting layers while employing a planar structure compatible with robust wafer-scale growth and fabrication.

While our multi-heterostructure does not have the highest visible broadband absorption of the reviewed publications, we have achieved the highest broadband absorption in a semiconductor stack <10 nm thickness. Our device is simultaneously the thinnest by active material and most energy-dense by volume in the field, to the best of our knowledge. The reduced material usage, enhanced physical flexibility, and feasible scalability of an optimized ultrathin active absorber will open doors for an array of optoelectronic applications from photovoltaics (wearable electronics, aerospace, portable charging, etc.)[72] to sensing and stealth technology.[73]

To elucidate the potential of our ultrathin absorber in photovoltaic (PV) applications, we consider the design of a separate contact PV cell seen in Figure 5a by using a combined optoelectronic model. Silver and gold electrodes with a thickness of 0.01 μm and n- and p-regions with widths of 0.01 μm are used. The excitonic effects that dominate TMDC PV behavior are accounted for as per our previous studies.[82] Experimentally demonstrated values for exciton diffusion length, radiative and nonradiative lifetimes, and binding energy of freestanding TMDC monolayers are used in the model and listed in Table S1. Note that binding energy is taken as 10% of the accepted exciton binding energy of a freestanding monolayer given that bandgap tuning to this extent has been demonstrated through the Coulomb engineering of the localized dielectric environment.[83] More details about the simulations conducted can be found in Table S2.

The performance of the ultrathin PV is optimized for Figures 5b and 5c. Power conversion efficiency (PCE) scales with absorption, with the top layer $MoTe_2$ and second layer WS_2 being the largest contributors to J_{SC} and V_{OC}, respectively; this is expected from the high photocurrent generated in the top layer of the SL and the large bandgap in the WS_2. The IV curves for the $N = 4$ cell are provided in Figure S13. We thus calculate a PCE of 14.05% for the $N = 4$ SL and 15.54% for the $N = 5$, under AM 1.5 normal incidence. This performance can be benchmarked against other leading material classes for ultrathin PVs, such as organic PVs (OPVs) and perovskites.[84,85] In Figure 5d, the metric of the specific power is used. This is calculated by dividing the converted integrated spectrum power at AM 1.5 for the device by its effective thickness, with more details on calculation provided in the Supporting Information. As seen, the $N = 4$ and $N = 5$ SL have specific densities of 291.6 and 311.4 W g^{-1}, respectively, >2 times higher than the next leading technology, to the best of our knowledge. This is due to the outstanding excitonic properties of TMDC-based PVs[82] and ultrathin nature of our material at 2.8 nm ($N = 4$) and 3.5 nm ($N = 5$) of active thickness, <60 nm of effective thickness, and <0.5 g m^{-2} of weight.

In summary, we have presented scalable TMDC-based multi-heterostructures using five different monolayer TMDCs as light-trapping layers. The incorporation of the various electronically isolated TMDCs contributes to multiple excitonic resonant peaks within the same structure, ultimately achieving >70% average total broadband absorption in the 450−700 nm visible range in a multi-heterostructure using 3.5 nm of active material. Further, the multi-heterostructure is predicted to have a power conversion efficiency of 15.54% and a specific power of over 300 W g^{-1} in a separate contact model

https://doi.org/10.1021/acs.nanolett.4c02963
Nano Lett. 2024, 24, 13935−13944

optimized for excitonic effects. Our study presents a robust, scalable, and realistic approach to engineering broadband semiconductor absorbers on arbitrary surfaces with versatile potential applications in photovoltaics, sensing, integrated circuits, displays, and more.

■ ASSOCIATED CONTENT

Supporting Information

The Supporting Information is available free of charge at https://pubs.acs.org/doi/10.1021/acs.nanolett.4c02963.

Experimental procedures, including optical simulations, multi-heterostructure characterization, and photovoltaic simulations; device optimization, including refractive indices, optimization or dielectrics, and layer thicknesses; device characterization, including transfer process effects, SEM/TEM, PL spectra, and Raman spectra; and solar cell simulations, including design parameters, TMDC-dependent performance, solar absorptance, and $I-V$ curves (PDF)

■ AUTHOR INFORMATION

Corresponding Author

Deep Jariwala − *Materials Science and Engineering and Electrical and Systems Engineering, University of Pennsylvania, Philadelphia, Pennsylvania 19104, United States;* orcid.org/0000-0002-3570-8768; Email: dmj@seas.upenn.edu

Authors

Da Lin − *Materials Science and Engineering, University of Pennsylvania, Philadelphia, Pennsylvania 19104, United States*

Jason Lynch − *Electrical and Systems Engineering, University of Pennsylvania, Philadelphia, Pennsylvania 19104, United States*

Sudong Wang − *Electrical and Systems Engineering, University of Pennsylvania, Philadelphia, Pennsylvania 19104, United States*

Zekun Hu − *Electrical and Systems Engineering, University of Pennsylvania, Philadelphia, Pennsylvania 19104, United States*

Rajeev Kumar Rai − *Materials Science and Engineering, University of Pennsylvania, Philadelphia, Pennsylvania 19104, United States;* orcid.org/0000-0002-2248-7601

Huairuo Zhang − *Materials Science and Engineering Division, National Institute of Standards and Technology, Gaithersburg, Maryland 208999, United States; Theiss Research, Inc., La Jolla, California 92037, United States;* orcid.org/0000-0002-1984-1200

Chen Chen − *2D Crystal Consortium Materials Innovation Platform, Materials Research Institute, Penn State University, University Park, Pennsylvania 16802, United States; Department of Materials Science and Engineering, 2D Crystal Consortium Materials Innovation Platform, Materials Research Institute, Pennsylvania State University, University Park, Pennsylvania 16801, United States*

Shalini Kumari − *2D Crystal Consortium Materials Innovation Platform, Materials Research Institute, Penn State University, University Park, Pennsylvania 16802, United States; Department of Materials Science and Engineering, 2D Crystal Consortium Materials Innovation Platform, Materials Research Institute, Pennsylvania State University, University Park, Pennsylvania 16801, United States;* orcid.org/0000-0001-6457-2858

Eric A. Stach − *Materials Science and Engineering, University of Pennsylvania, Philadelphia, Pennsylvania 19104, United States;* orcid.org/0000-0002-3366-2153

Albert V. Davydov − *Materials Science and Engineering Division, National Institute of Standards and Technology, Gaithersburg, Maryland 208999, United States*

Joan M. Redwing − *2D Crystal Consortium Materials Innovation Platform, Materials Research Institute and Materials Science and Engineering, Penn State University, University Park, Pennsylvania 16802, United States; Department of Materials Science and Engineering, 2D Crystal Consortium Materials Innovation Platform, Materials Research Institute, Pennsylvania State University, University Park, Pennsylvania 16801, United States;* orcid.org/0000-0002-7906-452X

Complete contact information is available at: https://pubs.acs.org/10.1021/acs.nanolett.4c02963

Notes

The authors declare no competing financial interest.

■ ACKNOWLEDGMENTS

The authors acknowledge primary support from the Office of Naval Research (ONR) Young Investigator Award (YIP) (N00014-23-1-203) Metamaterials Program. The authors thank Adam Alfieri for his work on the alignment markers for XTEM. D.J. also acknowledges support from the Alfred P. Sloan Foundation's Sloan Fellowship in Chemistry. D.L. acknowledges support from the Penn Engineering Rachleff Scholars Program and University of Pennsylvania Center for Undergraduate Research & Fellowships Grants for Faculty Mentoring Undergraduate Research (GfFMUR). H.Z. acknowledges support from the U.S. Department of Commerce, NIST under financial assistance awards 70NANB22H101 and 70NANB22H075. The MOCVD grown TMDC monolayer samples were provided by the 2D Crystal Consortium Materials Innovation Platform (2DCC-MIP) facility at Penn State, which is funded by the NSF under cooperative agreement DMR-2039351. This work was carried out in part at the Singh Center for Nanotechnology, which is supported by the NSF National Nanotechnology Coordinated Infrastructure Program under grant NNCI-2025608 and through the use of facilities supported by the University of Pennsylvania Materials Research Science and Engineering Center (MRSEC) DMR-2309043.

■ REFERENCES

(1) Sai, H.; Oku, T.; Sato, Y.; Tanabe, M.; Matsui, T.; Matsubara, K. Potential of Very Thin and High-efficiency Silicon Heterojunction Solar Cells. *Prog. Photovolt. Res. Appl.* **2019**, *27* (12), 1061−1070.

(2) Massiot, I.; Cattoni, A.; Collin, S. Progress and Prospects for Ultrathin Solar Cells. *Nat. Energy* **2020**, *5* (12), 959−972.

(3) Dotan, H.; Kfir, O.; Sharlin, E.; Blank, O.; Gross, M.; Dumchin, I.; Ankonina, G.; Rothschild, A. Resonant Light Trapping in Ultrathin Films for Water Splitting. *Nat. Mater.* **2013**, *12* (2), 158−164.

(4) Reece, S. Y.; Hamel, J. A.; Sung, K.; Jarvi, T. D.; Esswein, A. J.; Pijpers, J. J. H.; Nocera, D. G. Wireless Solar Water Splitting Using Silicon-Based Semiconductors and Earth-Abundant Catalysts. *Science* **2011**, *334* (6056), 645−648.

(5) Goldflam, M. D.; Kadlec, E. A.; Olson, B. V.; Klem, J. F.; Hawkins, S. D.; Parameswaran, S.; Coon, W. T.; Keeler, G. A.; Fortune, T. R.; Tauke-Pedretti, A.; Wendt, J. R.; Shaner, E. A.; Davids,

P. S.; Kim, J. K.; Peters, D. W. Enhanced Infrared Detectors Using Resonant Structures Combined with Thin Type-II Superlattice Absorbers. *Appl. Phys. Lett.* **2016**, *109* (25), 251103.
(6) Landy, N. I.; Sajuyigbe, S.; Mock, J. J.; Smith, D. R.; Padilla, W. J. Perfect Metamaterial Absorber. *Phys. Rev. Lett.* **2008**, *100* (20), No. 207402.
(7) Aydin, K.; Ferry, V. E.; Briggs, R. M.; Atwater, H. A. Broadband Polarization-Independent Resonant Light Absorption Using Ultrathin Plasmonic Super Absorbers. *Nat. Commun.* **2011**, *2* (1), 517.
(8) Li, W.; Guler, U.; Kinsey, N.; Naik, G. V.; Boltasseva, A.; Guan, J.; Shalaev, V. M.; Kildishev, A. V. Refractory Plasmonics with Titanium Nitride: Broadband Metamaterial Absorber. *Adv. Mater.* **2014**, *26* (47), 7959−7965.
(9) Deng, H.; Li, Z.; Stan, L.; Rosenmann, D.; Czaplewski, D.; Gao, J.; Yang, X. Broadband Perfect Absorber Based on One Ultrathin Layer of Refractory Metal. *Opt. Lett.* **2015**, *40* (11), 2592.
(10) Lei, L.; Li, S.; Huang, H.; Tao, K.; Xu, P. Ultra-Broadband Absorber from Visible to near-Infrared Using Plasmonic Metamaterial. *Opt. Express* **2018**, *26* (5), 5686.
(11) Li, J.; Chen, X.; Yi, Z.; Yang, H.; Tang, Y.; Yi, Y.; Yao, W.; Wang, J.; Yi, Y. Broadband Solar Energy Absorber Based on Monolayer Molybdenum Disulfide Using Tungsten Elliptical Arrays. *Mater. Today Energy* **2020**, *16*, No. 100390.
(12) Massiot, I.; Vandamme, N.; Bardou, N.; Dupuis, C.; Lemaître, A.; Guillemoles, J.-F.; Collin, S. Metal Nanogrid for Broadband Multiresonant Light-Harvesting in Ultrathin GaAs Layers. *ACS Photonics* **2014**, *1* (9), 878−884.
(13) Pala, R. A.; Butun, S.; Aydin, K.; Atwater, H. A. Omnidirectional and Broadband Absorption Enhancement from Trapezoidal Mie Resonators in Semiconductor Metasurfaces. *Sci. Rep.* **2016**, *6* (1), 31451.
(14) Tavakoli, N.; Spalding, R.; Lambertz, A.; Koppejan, P.; Gkantzounis, G.; Wan, C.; Röhrich, R.; Kontoleta, E.; Koenderink, A. F.; Sapienza, R.; Florescu, M.; Alarcon-Llado, E. Over 65% Sunlight Absorption in a 1 Mm Si Slab with Hyperuniform Texture. *ACS Photonics* **2022**, *9* (4), 1206−1217.
(15) Kats, M. A.; Blanchard, R.; Genevet, P.; Capasso, F. Nanometre Optical Coatings Based on Strong Interference Effects in Highly Absorbing Media. *Nat. Mater.* **2013**, *12* (1), 20−24.
(16) Alfieri, A. D.; Ruth, T.; Lim, C.; Lynch, J.; Jariwala, D. Self-Hybridized Exciton-Polariton Photovoltaics. *arXiv* June 18, 2024. DOI: 10.48550/arXiv.2406.13065 (accessed 2024-06-22).
(17) Du, W.; Yu, P.; Zhu, J.; Li, C.; Xu, H.; Zou, J.; Wu, C.; Wen, Q.; Ji, H.; Liu, T.; Li, Y.; Zou, G.; Wu, J.; Wang, Z. M. An Ultrathin $MoSe_2$ Photodetector with near-Perfect Absorption. *Nanotechnology* **2020**, *31* (22), 225201.
(18) Liu, D.; Yu, H.; Yang, Z.; Duan, Y. Ultrathin Planar Broadband Absorber through Effective Medium Design. *Nano Res.* **2016**, *9* (8), 2354−2363.
(19) Zhang, Y.; Liu, W.; Li, Z.; Cheng, H.; Zhang, Y.; Jia, G.; Chen, S.; Tian, J. Ultrathin Polarization-Insensitive Wide-Angle Broadband near-Perfect Absorber in the Visible Regime Based on Few-Layer MoS2 Films. *Appl. Phys. Lett.* **2017**, *111* (11), 111109.
(20) Liu, D.; Li, Q. Sub-Nanometer Planar Solar Absorber. *Nano Energy* **2017**, *34*, 172−180.
(21) Pirruccio, G.; Martin Moreno, L.; Lozano, G.; Gomez Rivas, J. Coherent and Broadband Enhanced Optical Absorption in Graphene. *ACS Nano* **2013**, *7* (6), 4810−4817.
(22) Kumar, P.; Lynch, J.; Song, B.; Ling, H.; Barrera, F.; Kisslinger, K.; Zhang, H.; Anantharaman, S. B.; Digani, J.; Zhu, H.; Choudhury, T. H.; McAleese, C.; Wang, X.; Conran, B. R.; Whear, O.; Motala, M. J.; Snure, M.; Muratore, C.; Redwing, J. M.; Glavin, N. R.; Stach, E. A.; Davoyan, A. R.; Jariwala, D. Light−Matter Coupling in Large-Area van Der Waals Superlattices. *Nat. Nanotechnol.* **2022**, *17* (2), 182−189.
(23) Elrafei, S. A.; Heijnen, L. M.; Godiksen, R. H.; Curto, A. G. Monolayer Semiconductor Superlattices with High Optical Absorption. *ACS Photonics* **2024**, *11* (7), 2587−2594.
(24) Imamoto, H.; Sato, F.; Imanaka, K.; Shimura, M. AlGaAs/GaAs Superlattice Multi-Quantum-Well Laser Diode. *Superlattices Microstruct.* **1989**, *5* (2), 167−170.
(25) Mak, K. F.; Lee, C.; Hone, J.; Shan, J.; Heinz, T. F. Atomically Thin MoS2: A New Direct-Gap Semiconductor. *Phys. Rev. Lett.* **2010**, *105* (13), No. 136805.
(26) Wang, G.; Chernikov, A.; Glazov, M. M.; Heinz, T. F.; Marie, X.; Amand, T.; Urbaszek, B. *Colloquium*: Excitons in Atomically Thin Transition Metal Dichalcogenides. *Rev. Mod. Phys.* **2018**, *90* (2), No. 021001.
(27) Gutiérrez, H. R.; Perea-López, N.; Elías, A. L.; Berkdemir, A.; Wang, B.; Lv, R.; López-Urías, F.; Crespi, V. H.; Terrones, H.; Terrones, M. Extraordinary Room-Temperature Photoluminescence in Triangular WS_2 Monolayers. *Nano Lett.* **2013**, *13* (8), 3447−3454.
(28) Desai, S. B.; Seol, G.; Kang, J. S.; Fang, H.; Battaglia, C.; Kapadia, R.; Ager, J. W.; Guo, J.; Javey, A. Strain-Induced Indirect to Direct Bandgap Transition in Multilayer WSe2. *Nano Lett.* **2014**, *14* (8), 4592−4597.
(29) Nie, Z.; Trovatello, C.; Pogna, E. A. A.; Dal Conte, S.; Miranda, P. B.; Kelleher, E.; Zhu, C.; Turcu, I. C. E.; Xu, Y.; Liu, K.; Cerullo, G.; Wang, F. Broadband Nonlinear Optical Response of Monolayer MoSe2 under Ultrafast Excitation. *Appl. Phys. Lett.* **2018**, *112* (3), 031108.
(30) Tonndorf, P.; Schmidt, R.; Bottger, P.; Zhang, X.; Borner, J.; Liebig, A.; Albrecht, M.; Kloc, C.; Gordan, O.; Zahn, D. R. T.; Michaelis de Vasconcellos, S.; Bratschitsch, R. Photoluminescence Emission and Raman Response of Monolayer MoS_2, MoSe_2, and WSe_2. *Opt. Express* **2013**, *21* (4), 4908.
(31) Ruppert, C.; Aslan, B.; Heinz, T. F. Optical Properties and Band Gap of Single- and Few-Layer $MoTe_2$ Crystals. *Nano Lett.* **2014**, *14* (11), 6231−6236.
(32) Ameri, T.; Dennler, G.; Lungenschmied, C.; Brabec, C. J. Organic Tandem Solar Cells: A Review. *Energy Environ. Sci.* **2009**, *2* (4), 347−363.
(33) Diaz, H. C.; Chaghi, R.; Ma, Y.; Batzill, M. Molecular Beam Epitaxy of the van Der Waals Heterostructure $MoTe_2$ on MoS_2: Phase, Thermal, and Chemical Stability. *2D Mater.* **2015**, *2* (4), No. 044010.
(34) Zhu, H.; Wang, Q.; Cheng, L.; Addou, R.; Kim, J.; Kim, M. J.; Wallace, R. M. Defects and Surface Structural Stability of $MoTe_2$ Under Vacuum Annealing. *ACS Nano* **2017**, *11* (11), 11005−11014.
(35) Xu, W.; Kozawa, D.; Zhou, Y.; Wang, Y.; Sheng, Y.; Jiang, T.; Strano, M. S.; Warner, J. H. Controlling Photoluminescence Enhancement and Energy Transfer in WS_2:hBN:WS_2 Vertical Stacks by Precise Interlayer Distances. *Small* **2020**, *16* (3), 1905985.
(36) Fang, H.; Battaglia, C.; Carraro, C.; Nemsak, S.; Ozdol, B.; Kang, J. S.; Bechtel, H. A.; Desai, S. B.; Kronast, F.; Unal, A. A.; Conti, G.; Conlon, C.; Palsson, G. K.; Martin, M. C.; Minor, A. M.; Fadley, C. S.; Yablonovitch, E.; Maboudian, R.; Javey, A. Strong Interlayer Coupling in van Der Waals Heterostructures Built from Single-Layer Chalcogenides. *Proc. Natl. Acad. Sci. U. S. A.* **2014**, *111* (17), 6198−6202.
(37) Hu, Z.; Hernández-Martínez, P. L.; Liu, X.; Amara, M.-R.; Zhao, W.; Watanabe, K.; Taniguchi, T.; Demir, H. V.; Xiong, Q. Trion-Mediated Förster Resonance Energy Transfer and Optical Gating Effect in WS2/hBN/MoSe2 Heterojunction. *ACS Nano* **2020**, *14* (10), 13470−13477.
(38) Yoon, Y.; Zhang, Z.; Qi, R.; Joe, A. Y.; Sailus, R.; Watanabe, K.; Taniguchi, T.; Tongay, S.; Wang, F. Charge Transfer Dynamics in MoSe2/hBN/WSe2 Heterostructures. *Nano Lett.* **2022**, *22* (24), 10140−10146.
(39) Shik, A. Y. *Quantum Wells: Physics and Electronics of Two-Dimensional Systems*; World Scientific, 1997.
(40) Yang, J.; Yoon, A.; Lee, D.; Song, S.; Jung, I. J.; Lim, D.-H.; Jeong, H.; Lee, Z.; Lanza, M.; Kwon, S.-Y. Wafer-Scale Memristor Array Based on Aligned Grain Boundaries of 2D Molybdenum Ditelluride for Application to Artificial Synapses. *Adv. Funct. Mater.* **2024**, *34*, 2309455.

(41) Holman, Z. C.; Filipic, M.; Lipovsek, B.; De Wolf, S.; Smole, F.; Topic, M.; Ballif, C. Parasitic Absorption in the Rear Reflector of a Silicon Solar Cell: Simulation and Measurement of the Sub-Bandgap Reflectance for Common Dielectric/Metal Reflectors. *Sol. Energy Mater. Sol. Cells* **2014**, *120*, 426−430.
(42) Huang, Y.; Pan, Y.-H.; Yang, R.; Bao, L.-H.; Meng, L.; Luo, H.-L.; Cai, Y.-Q.; Liu, G.-D.; Zhao, W.-J.; Zhou, Z.; Wu, L.-M.; Zhu, Z.-L.; Huang, M.; Liu, L.-W.; Liu, L.; Cheng, P.; Wu, K.-H.; Tian, S.-B.; Gu, C.-Z.; Shi, Y.-G.; Guo, Y.-F.; Cheng, Z. G.; Hu, J.-P.; Zhao, L.; Yang, G.-H.; Sutter, E.; Sutter, P.; Wang, Y.-L.; Ji, W.; Zhou, X.-J.; Gao, H.-J. Universal Mechanical Exfoliation of Large-Area 2D Crystals. *Nat. Commun.* **2020**, *11* (1), 2453.
(43) Lu, Z.; Sun, L.; Xu, G.; Zheng, J.; Zhang, Q.; Wang, J.; Jiao, L. Universal Transfer and Stacking of Chemical Vapor Deposition Grown Two-Dimensional Atomic Layers with Water-Soluble Polymer Mediator. *ACS Nano* **2016**, *10* (5), 5237−5242.
(44) Li, H.; Yin, Z.; He, Q.; Li, H.; Huang, X.; Lu, G.; Fam, D. W. H.; Tok, A. I. Y.; Zhang, Q.; Zhang, H. Fabrication of Single- and Multilayer MoS_2 Film-Based Field-Effect Transistors for Sensing NO at Room Temperature. *Small* **2012**, *8* (1), 63−67.
(45) Sebastian, A.; Pendurthi, R.; Choudhury, T. H.; Redwing, J. M.; Das, S. Benchmarking Monolayer MoS2 and WS2 Field-Effect Transistors. *Nat. Commun.* **2021**, *12* (1), 693.
(46) Kim, T.; Park, H.; Joung, D.; Kim, D.; Lee, R.; Shin, C. H.; Diware, M.; Chegal, W.; Jeong, S. H.; Shin, J. C.; Park, J.; Kang, S.-W. Wafer-Scale Epitaxial 1T′, 1T′−2H Mixed, and 2H Phases MoTe2 Thin Films Grown by Metal−Organic Chemical Vapor Deposition. *Adv. Mater. Interfaces* **2018**, *5* (15), 1800439.
(47) Choudhury, T. H.; Zhang, X.; Al Balushi, Z. Y.; Chubarov, M.; Redwing, J. M. Epitaxial Growth of Two-Dimensional Layered Transition Metal Dichalcogenides. *Annu. Rev. Mater. Res.* **2020**, *50*, 155−177.
(48) Kuc, A.; Zibouche, N.; Heine, T. Influence of Quantum Confinement on the Electronic Structure of the Transition Metal Sulfide TS2. *Phys. Rev. B* **2011**, *83* (24), No. 245213.
(49) Yun, W. S.; Han, S. W.; Hong, S. C.; Kim, I. G.; Lee, J. D. Thickness and Strain Effects on Electronic Structures of Transition Metal Dichalcogenides: 2H-MX2 Semiconductors (M = Mo, W; X = S, Se, Te). *Phys. Rev. B* **2012**, *85* (3), No. 033305.
(50) Zhu, M.; Zhang, Z.; Zhang, T.; Liu, D.; Zhang, H.; Zhang, Z.; Li, Z.; Cheng, Y.; Huang, W. Exchange between Interlayer and Intralayer Exciton in WSe_2 /WS_2 Heterostructure by Interlayer Coupling Engineering. *Nano Lett.* **2022**, *22* (11), 4528−4534.
(51) Mouri, S.; Miyauchi, Y.; Matsuda, K. Tunable Photoluminescence of Monolayer MoS_2 via Chemical Doping. *Nano Lett.* **2013**, *13* (12), 5944−5948.
(52) Ghosh, C. K.; Sarkar, D.; Mitra, M. K.; Chattopadhyay, K. K. Equibiaxial Strain: Tunable Electronic Structure and Optical Properties of Bulk and Monolayer $MoSe_2$. *J. Phys. Appl. Phys.* **2013**, *46* (39), No. 395304.
(53) Raja, A.; Waldecker, L.; Zipfel, J.; Cho, Y.; Brem, S.; Ziegler, J. D.; Kulig, M.; Taniguchi, T.; Watanabe, K.; Malic, E.; Heinz, T. F.; Berkelbach, T. C.; Chernikov, A. Dielectric Disorder in Two-Dimensional Materials. *Nat. Nanotechnol.* **2019**, *14* (9), 832−837.
(54) Mohamed, N. B.; Lim, H. E.; Wang, F.; Koirala, S.; Mouri, S.; Shinokita, K.; Miyauchi, Y.; Matsuda, K. Long Radiative Lifetimes of Excitons in Monolayer Transition-Metal Dichalcogenides MX_2 (M = Mo, W; X = S, Se). *Appl. Phys. Express* **2018**, *11* (1), No. 015201.
(55) Roy, S.; Sharbirin, A. S.; Lee, Y.; Kim, W. B.; Kim, T. S.; Cho, K.; Kang, K.; Jung, H. S.; Kim, J. Measurement of Quantum Yields of Monolayer TMDs Using Dye-Dispersed PMMA Thin Films. *Nanomaterials* **2020**, *10* (6), 1032.
(56) Cui, Q.; Luo, Z.; Cui, Q.; Zhu, W.; Shou, H.; Wu, C.; Liu, Z.; Lin, Y.; Zhang, P.; Wei, S.; Yang, H.; Chen, S.; Pan, A.; Song, L. Robust and High Photoluminescence in WS_2 Monolayer through In Situ Defect Engineering. *Adv. Funct. Mater.* **2021**, *31* (38), 2105339.
(57) Wang, J.; Liu, H.; Hu, X.; Liu, Y.; Liu, D. Imaging of Defect-Accelerated Energy Transfer in MoS_2 /hBN/WS_2 Heterostructures. *ACS Appl. Mater. Interfaces* **2022**, *14* (6), 8521−8526.
(58) Li, X.; Puretzky, A. A.; Sang, X.; KC, S.; Tian, M.; Ceballos, F.; Mahjouri-Samani, M.; Wang, K.; Unocic, R. R.; Zhao, H.; Duscher, G.; Cooper, V. R.; Rouleau, C. M.; Geohegan, D. B.; Xiao, K. Suppression of Defects and Deep Levels Using Isoelectronic Tungsten Substitution in Monolayer $MoSe_2$. *Adv. Funct. Mater.* **2017**, *27* (19), 1603850.
(59) Kumar, D.; Kumar, V.; Kumar, R.; Kumar, M.; Kumar, P. Electron-Phonon Coupling, Thermal Expansion Coefficient, Resonance Effect, and Phonon Dynamics in High-Quality CVD-Grown Monolayer and Bilayer MoSe2. *Phys. Rev. B* **2022**, *105* (8), No. 085419.
(60) Bauccio, M. *ASM Engineered Materials Reference Book*, 2nd ed.; ASM International, 1994.
(61) Zhang, D.; Wu, Y.-C.; Yang, M.; Liu, X.; Coileáin, C. Ó.; Xu, H.; Abid, M.; Abid, M.; Wang, J.-J.; Shvets, I. V.; Liu, H.; Wang, Z.; Yin, H.; Liu, H.; Chun, B. S.; Zhang, X.; Wu, H.-C. Probing Thermal Expansion Coefficients of Monolayers Using Surface Enhanced Raman Scattering. *RSC Adv.* **2016**, *6* (101), 99053−99059.
(62) Morell, N.; Reserbat-Plantey, A.; Tsioutsios, I.; Schädler, K. G.; Dubin, F.; Koppens, F. H. L.; Bachtold, A. High Quality Factor Mechanical Resonators Based on WSe_2 Monolayers. *Nano Lett.* **2016**, *16* (8), 5102−5108.
(63) Zhang, L.; Lu, Z.; Song, Y.; Zhao, L.; Bhatia, B.; Bagnall, K. R.; Wang, E. N. Thermal Expansion Coefficient of Monolayer Molybdenum Disulfide Using Micro-Raman Spectroscopy. *Nano Lett.* **2019**, *19* (7), 4745−4751.
(64) Lee, C.; Yan, H.; Brus, L. E.; Heinz, T. F.; Hone, J.; Ryu, S. Anomalous Lattice Vibrations of Single- and Few-Layer MoS_2. *ACS Nano* **2010**, *4* (5), 2695−2700.
(65) Berkdemir, A.; Gutiérrez, H. R.; Botello-Méndez, A. R.; Perea-López, N.; Elías, A. L.; Chia, C.-I.; Wang, B.; Crespi, V. H.; López-Urías, F.; Charlier, J.-C.; Terrones, H.; Terrones, M. Identification of Individual and Few Layers of WS2 Using Raman Spectroscopy. *Sci. Rep.* **2013**, *3* (1), 1755.
(66) Zhang, W.; Huang, J.-K.; Chen, C.-H.; Chang, Y.-H.; Cheng, Y.-J.; Li, L.-J. High-Gain Phototransistors Based on a CVD MoS2Monolayer. *Adv. Mater.* **2013**, *25* (25), 3456−3461.
(67) Ye, Z.; Cao, T.; O'Brien, K.; Zhu, H.; Yin, X.; Wang, Y.; Louie, S. G.; Zhang, X. Probing Excitonic Dark States in Single-Layer Tungsten Disulphide. *Nature* **2014**, *513* (7517), 214−218.
(68) Mattheiss, L. F. Band Structures of Transition-Metal-Dichalcogenide Layer Compounds. *Phys. Rev. B* **1973**, *8* (8), 3719−3740.
(69) Pettersson, L. A. A.; Roman, L. S.; Inganäs, O. Modeling Photocurrent Action Spectra of Photovoltaic Devices Based on Organic Thin Films. *J. Appl. Phys.* **1999**, *86* (1), 487−496.
(70) Jariwala, D.; Davoyan, A. R.; Wong, J.; Atwater, H. A. Van Der Waals Materials for Atomically-Thin Photovoltaics: Promise and Outlook. *ACS Photonics* **2017**, *4* (12), 2962−2970.
(71) Cao, J.; Wang, J.; Yang, G.; Lu, Y.; Sun, R.; Yan, P.; Gao, S. Enhancement of Broad-Band Light Absorption in Monolayer MoS2 Using Ag Grating Hybrid with Distributed Bragg Reflector. *Superlattices Microstruct.* **2017**, *110*, 26−30.
(72) Reese, M. O.; Glynn, S.; Kempe, M. D.; McGott, D. L.; Dabney, M. S.; Barnes, T. M.; Booth, S.; Feldman, D.; Haegel, N. M. Increasing Markets and Decreasing Package Weight for High-Specific-Power Photovoltaics. *Nat. Energy* **2018**, *3* (11), 1002−1012.
(73) Yu, P.; Besteiro, L. V.; Huang, Y.; Wu, J.; Fu, L.; Tan, H. H.; Jagadish, C.; Wiederrecht, G. P.; Govorov, A. O.; Wang, Z. Broadband Metamaterial Absorbers. *Adv. Opt. Mater.* **2019**, *7* (3), 1800995.
(74) Park, J.; Kang, J.-H.; Vasudev, A. P.; Schoen, D. T.; Kim, H.; Hasman, E.; Brongersma, M. L. Omnidirectional Near-Unity Absorption in an Ultrathin Planar Semiconductor Layer on a Metal Substrate. *ACS Photonics* **2014**, *1* (9), 812−821.
(75) He, J.; Chen, C.; Liu, W.; Zhu, X.; Zheng, Y.; Wang, S.; Chen, L.; Zhang, R. Enhanced Broadband Light Absorption of Ultrathin $PtSe_2$ in Metal−Insulator−Metal Structure. *J. Phys. Appl. Phys.* **2023**, *56* (39), 395102.

https://doi.org/10.1021/acs.nanolett.4c02963
Nano Lett. 2024, 24, 13935−13944

(76) Tang, P.; Liu, G.; Liu, X.; Fu, G.; Liu, Z.; Wang, J. Plasmonic Wavy Surface for Ultrathin Semiconductor Black Absorbers. *Opt. Express* **2020**, *28* (19), 27764.
(77) Huang, L.-J.; Li, J.-Q.; Lu, M.-Y.; Chen, Y.-Q.; Zhu, H.-J.; Liu, H.-Y. Broadband Visible Light Absorber Based on Ultrathin Semiconductor Nanostructures*. *Chin. Phys. B* **2020**, *29* (1), No. 014201.
(78) Qian, Q.; Sun, T.; Yan, Y.; Wang, C. Large-Area Wide-Incident-Angle Metasurface Perfect Absorber in Total Visible Band Based on Coupled Mie Resonances. *Adv. Opt. Mater.* **2017**, *5* (13), 1700064.
(79) Lee, K.-T.; Ji, C.; Guo, L. J. Wide-Angle, Polarization-Independent Ultrathin Broadband Visible Absorbers. *Appl. Phys. Lett.* **2016**, *108* (3), No. 031107.
(80) Wu, S.; Ye, Y.; Luo, M.; Chen, L. Ultrathin Omnidirectional, Broadband Visible Absorbers. *J. Opt. Soc. Am. B* **2018**, *35* (8), 1825.
(81) Hashemi, M.; Ansari, N.; Vazayefi, M. MoS2-Based Absorbers with Whole Visible Spectrum Coverage and High Efficiency. *Sci. Rep.* **2022**, *12* (1), 6313.
(82) Hu, Z.; Lin, D.; Lynch, J.; Xu, K.; Jariwala, D. How Good Can 2D Excitonic Solar Cells Be? *Device* **2023**, *1* (1), No. 100003.
(83) Raja, A.; Chaves, A.; Yu, J.; Arefe, G.; Hill, H. M.; Rigosi, A. F.; Berkelbach, T. C.; Nagler, P.; Schüller, C.; Korn, T.; Nuckolls, C.; Hone, J.; Brus, L. E.; Heinz, T. F.; Reichman, D. R.; Chernikov, A. Coulomb Engineering of the Bandgap and Excitons in Two-Dimensional Materials. *Nat. Commun.* **2017**, *8* (1), 15251.
(84) Xiong, S.; Fukuda, K.; Lee, S.; Nakano, K.; Dong, X.; Yokota, T.; Tajima, K.; Zhou, Y.; Someya, T. Ultrathin and Efficient Organic Photovoltaics with Enhanced Air Stability by Suppression of Zinc Element Diffusion. *Adv. Sci.* **2022**, *9* (8), 2105288.
(85) Kaltenbrunner, M.; Adam, G.; Głowacki, E. D.; Drack, M.; Schwödiauer, R.; Leonat, L.; Apaydin, D. H.; Groiss, H.; Scharber, M. C.; White, M. S.; Sariciftci, N. S.; Bauer, S. Flexible High Power-per-Weight Perovskite Solar Cells with Chromium Oxide−Metal Contacts for Improved Stability in Air. *Nat. Mater.* **2015**, *14* (10), 1032−1039.
(86) Gupta, A.; Parikh, V.; Compaan, A. D. High Efficiency Ultra-Thin Sputtered CdTe Solar Cells. *Sol. Energy Mater. Sol. Cells* **2006**, *90* (15), 2263−2271.
(87) Zhao, F.; Lin, J.; Lei, Z.; Yi, Z.; Qin, F.; Zhang, J.; Liu, L.; Wu, X.; Yang, W.; Wu, P. Realization of 18.97% Theoretical Efficiency of 0.9 Mm Thick c-Si/ZnO Heterojunction Ultrathin-Film Solar Cells *via* Surface Plasmon Resonance Enhancement. *Phys. Chem. Chem. Phys.* **2022**, *24* (8), 4871−4880.
(88) Buencuerpo, J.; Saenz, T. E.; Steger, M.; Young, M.; Warren, E. L.; Geisz, J. F.; Steiner, M. A.; Tamboli, A. C. Efficient Light-Trapping in Ultrathin GaAs Solar Cells Using Quasi-Random Photonic Crystals. *Nano Energy* **2022**, *96*, No. 107080.

https://doi.org/10.1021/acs.nanolett.4c02963
Nano Lett. 2024, 24, 13935−13944